INSTITUTE OF PHYSICS PUBLISHING PLASMA SOURCES SCIENCE AND TECHNOLOGY
Plasma Sources Sci. Technol. **10** (2001) 595–605 PII: S0963-0252(01)28408-4

Flow dynamics and invasion by background gas of a supersonically expanding thermal plasma

R Engeln[1,3], **S Mazouffre**[1], **P Vankan**[1], **D C Schram**[1] **and N Sadeghi**[2]

[1]Department of Applied Physics, Centre for Plasma Physics and Radiation Technology (CPS), Eindhoven University of Technology, PO Box 513, 5600 MB Eindhoven, The Netherlands
[2]Laboratoire de Spectrometrie Physique, UMR C5588, Université Joseph Fourier-Grenoble I, F-38402 St Martin d'Heres cedex, France

E-mail: r.engeln@phys.tue.nl

Received 20 April 2001, in final form 13 August 2001
Published 2 October 2001
Online at stacks.iop.org/PSST/10/595

Abstract
The transport of neutral argon atoms in an expanding thermal argon/hydrogen plasma is studied by means of laser-induced fluorescence spectroscopy around 811 nm, on the long living Ar[4s] atoms. Although the Doppler shifted laser-induced fluorescence measurements are performed on argon atoms in the metastable $Ar^*(^3P_2)$ and resonant $Ar^*(^3P_1)$ states, it is argued that in the plasma jet the velocity distribution function of these Ar[4s] atoms images the velocity distribution functions of the ground-state argon atoms. From the results it is inferred that the velocity behaviour of the supersonically expanding argon gas can be predicted from the momentum balance, and the temperature from the adiabatic relation between density and temperature. However, the adiabatic constant is found to be 1.4 ± 0.1, smaller than the adiabatic constant of a neutral argon gas expansion which is $\frac{5}{3}$. Both in the axial and in the radial directions the velocity distributions measured in the shock region show clear departures from thermodynamic equilibrium. From the radial velocity distribution it is concluded that background gas invades the supersonic part of the expanding plasma jet. The results on temperature and velocity in the subsonic region show that the radius of the plasma jet hardly increases after the stationary shock front, indicating that the flow pattern is geometrically determined.

1. Introduction

Expanding thermal plasmas are interesting both from a fundamental point of view as well as from considerations of applicability. From a fundamental point of view, the plasma expansion is the basis for describing phenomena ranging from astrophysical objects and solar flares, the flow into the divertor region of a Tokamak, to laser spots and vacuum arc spots [1–4]. In view of the applicability, expanding thermal plasmas are used for thin film deposition, etching, passivation and treatment of archaeological artifacts [5]. In these cases optimal energy conversion from the plasma source, via the expanding plasma to the gases used for surface modification or treatment, is of eminent importance. The study of the expansion can substantiate the understanding of the conversion process.

Over the recent past, extensive studies have been performed on expanding plasmas. Examples are Thomson–Rayleigh scattering measurements on the expansion properties of pure argon plasmas and argon/hydrogen plasmas, which supplied electron and neutral densities and electron temperatures [6–9]. Coherent anti-Stokes Raman scattering experiments on argon/hydrogen plasmas gave absolute densities of rovibrationally excited H_2 showing the importance of wall association and the recirculation of background

[3] Author to whom all correspondence should be addressed.

gas [10]. In a study on the influence of wall recombination processes on the transport of radicals, two-photon laser-induced fluorescence measurements on hydrogen atoms in an argon/hydrogen plasma were performed and atomic radical densities, temperatures and velocities were obtained [11–13]. These studies give a good insight into the physics of the expanding plasma, like recombination, excitation, wall association and recirculation, to just name a few.

Starting from a remote 'ionizing' plasma source, the plasma supersonically expands and very quickly becomes 'recombining'. The supersonic domain ends in the formation of a stationary shock wave. Behind this shock wave the plasma flows subsonically into the background. In the downstream region of the plasma expansion molecules, e.g. SiH_4, CH_4 or C_2H_2, can be injected into the plasma jet [14]. Here they are fragmented via charge exchange and dissociative recombination reactions into radicals. These molecular radicals are transported by the plasma flow to the substrate. At the substrate they can stick to the surface and contribute to film growth, reflect from the surface or recombine at the surface forming 'new' species. In the pressure range investigated, the residence time of the gases in the vessel (about 0.5 s at 20 Pa) is much longer than the circulation time. Thus newly formed species at walls can recirculate and subsequently influence the plasma in the vessel. The understanding of the mixing of the injected monomers and the newly formed molecules with the plasma jet is important for the optimal use of these species in deposition and etching processes.

In most of the studies and applications of the expanding plasma jet, argon is used as a carrier gas. Due to the relatively high mass, as compared with injected gases like hydrogen, nitrogen or methane, the velocity with which the plasma expands will be to a large extent determined by the Ar velocity. We report here on laser-induced fluorescence measurements on metastable argon atoms in an expanding thermal plasma generated from a mixture of argon with a few per cent of hydrogen. From these measurements both the axial and radial velocity components and temperatures of the neutral argon atoms are extracted. The velocity distribution in the shock region shows a clear departure from thermodynamic equilibrium, i.e. they cannot be described with a single Gaussian. It will be shown that the velocity and temperature in the supersonic region of the plasma expansion can be described as a neutral gas expansion with a modified value of the adiabatic exponent γ. Evidence of the penetration of the background gas in the supersonic part of the plasma expansion will be discussed.

2. Theoretical description of the expansion

The expansion of a thermal plasma can to a large extent be described with a formalism similar to the formalism used to describe the expansion of a neutral gas by Ashkenas and Sherman [15]. In both cases the gas flows from a high-pressure (p_0) region into a low-pressure (p_{bg}) vessel through an orifice, the so-called nozzle. In case the pressure ratio of the high- and low-pressure regions is larger than 2.1, the velocity w_z at the exit of the nozzle will equal the local sound velocity c_s, i.e. Mach number M equal to one [16]. The sound velocity is given by

$$c_s = \sqrt{\gamma \frac{k_B T}{m}}. \tag{1}$$

In this equation m is the mass of the gas particles, γ is the adiabatic exponent, which is the ratio of specific heat at constant pressure and volume (c_p/c_v), T the local temperature and k_B the Boltzmann constant. From the nozzle exit the gas accelerates along stream lines into the low-pressure region. Since the entropy has to be constant along a stream line, the gas temperature decreases, while the velocity increases. At a distance from the exit corresponding to a few times the diameter of the nozzle, the velocity reaches its maximum value, which can be expressed in terms of the sound velocity at the nozzle exit and γ (*vide infra*). At a certain position the expanding gas has to adjust to the background conditions. Since the gas is moving faster than the speed of sound, it does not 'sense' the boundary conditions [16], and the adjustment is made via the formation of a shock-wave structure. The shock on the side of the supersonic part of the expansion is called the barrel shock. The plane normal to the expansion axis where $M = 1$ is called the Mach disk. Behind the shock wave the gas flows subsonically into the background gas at constant static pressure.

2.1. The supersonic expansion

In the supersonic part of the expansion the density $n(z)$ decreases quadratically with increasing distance from the source z, due to an increase in the jet diameter;

$$n(z) = \frac{n_0}{1 + (z/z_0)^2}. \tag{2}$$

Here n_0 equals the density at $z = 0$. In (2) z_0 is a scaling length, introduced to allow for a comparison of measurements with nozzles with different diameters ($z_0/d \approx 0.5$). For values of z of the order of z_0 and smaller than z_0, equation (2) differs from that used by, e.g. Ashkenas and Sherman [15] and van de Sanden *et al* [6]. Their density relations show a discontinuity at $z = z_0$. Equation (2) however, allows for the coupling of independent calculations of source and expansion characteristics. Also, in the present situation the expansion of a flowing plasma (at sonic speed at the exit of the arc channel) is studied [17] rather than the expansion from a reservoir[4]. For $z \gg z_0$ both equations show the same dependence. Thomson and Rayleigh measurements of van de Sanden *et al* [6] and Meulenbroeks *et al* [9] on an argon and argon/hydrogen (2 to 5% hydrogen in argon) expanding thermal plasma show the validity of this equation.

Close to the nozzle the density decreases in the radial direction from the centre of the jet to the outside ('hill'-like structure, $n_{jet}^{on\text{-}axis} > n_{bg}$). However, further away from the nozzle the hill-like structure gradually weakens and can eventually go over into a 'valley'-like structure ($n_{jet}^{on\text{-}axis} < n_{bg}$), the so-called overexpanded region. In this region the static pressure is significantly lower than the background pressure, but the stagnation pressure is still higher.

[4] This allows for the use of the flux density relation $n(z)w_z = n_0 w_{z_0}/[1 + (z/z_0)^2]$.

Assuming an adiabatic expansion, the energy equation reduces to Poisson's adiabatic law

$$\frac{T(z)}{T_0} = \left(\frac{n(z)}{n_0}\right)^{\gamma-1}. \tag{3}$$

From a simplified momentum balance (no viscosity, no Lorentz forces) and assuming an adiabatic expansion, the following relation for the velocity w_z on the jet axis can be deduced [18]

$$w_z = c_{s_0}\left\{1 + \frac{2}{\gamma-1}\left[1 - \left(\frac{1}{1+(z/z_0)^2}\right)^{\gamma-1}\right]\right\}^{1/2}. \tag{4}$$

In (3) and (4) T_0 and c_{s_0} denote, respectively, the temperature and the sound velocity at the nozzle exit ($z = 0$). We assume $M = 1$ at the nozzle exit. From (4) it can be shown that the velocity of the expanding gas cannot exceed $w_{\max}$ [18]

$$w_{\max} = c_{s_0}\sqrt{\frac{\gamma+1}{\gamma-1}} \tag{5}$$

and that $w_{\max}$ is reached after a few diameters of the exit nozzle. This means that the mass and the heat capacity of the expanding gas mixture and the temperature at the nozzle exit, T_0, determine the maximum velocity to which the gas mixture can be accelerated (see also (1)).

2.2. The stationary shock wave

The stationary shock wave is defined as the area where a supersonic flow transforms into a subsonic flow. The plasma-flow parameters like density, temperature and velocity in front of and behind the stationary shock wave are related via the conservation laws for mass, momentum and energy. With the assumption that the forward flux is conserved through the shock wave, jump relations can be deduced for the density, temperature and velocity in front of and behind the shock [18]

$$\frac{w_1}{w_2} = \frac{n_2}{n_1} = \frac{(\gamma+1)M_1^2}{(\gamma-1)M_1^2+2} \tag{6}$$

$$\frac{T_2}{T_1} = \frac{[2\gamma M_1^2 - (\gamma-1)][(\gamma-1)M_1^2+2]}{(\gamma+1)^2 M_1^2}. \tag{7}$$

The subscripts 1 and 2 denote the quantities ahead of and behind the shock, respectively. Although these Rankine–Hugoniot relations are valid for infinitely narrow shock waves, it has been shown that they are still applicable in the case of finite shock wave thickness. This finite thickness arises from broadening mechanisms like viscosity and heat conduction. The thickness of the shock wave is of the order of the mean free path for neutral–neutral collisions, ahead of the shock front [18]. Van de Sanden *et al* [6] have shown the validity of this approach to describe the heavy-particle density jump through the stationary shock wave for an expanding thermal argon plasma.

Under our experimental conditions, in the overexpanded region the mean free path for neutral–neutral collisions is a significant fraction of the dimension of the plasma jet. This necessitates the use of a kinetic approach, on the basis of the Boltzmann transport equation, leading to the description of the density evolution through the shock wave. Several authors have shown that by assuming a bimodal velocity distribution function, an approximate solution of the Boltzmann transport equation is obtained [19–21].

In section 4 it will be shown that the decomposition of the non-Maxwellian distribution function, measured across the shock wave, into two Maxwellian distribution functions, leads to interesting new insights into the flow dynamics of this transition region.

2.3. The subsonic expansion

Behind the shock wave the plasma expands subsonically into the background. Measurements of van de Sanden and Meulenbroeks showed that the static pressure hardly changes in the subsonic part of the jet. Our measurements show that the ratio of the velocity and the temperature as a function of the position along the jet centre line is constant. Assuming that the flux is conserved and the density is inversely proportional to the temperature (at constant pressure), this leads to the conclusion that to a good approximation the beam width stays constant in the subsonic part. This is to be expected if the flow pattern is determined by the geometry of the vessel. In the centre the stream lines are parallel and are surrounded by a recirculation vortex. This has also been observed in simulations performed with PHOENICS [22].

3. The experimental setup

The experimental setup in which the expanding thermal plasma jet is created has been extensively described elsewhere [23]. Here, only a short description is given. A cascaded arc, operating at sub-atmospheric pressure (0.6 bar), produces a thermal plasma (source temperature $\hat{T}_s \approx 0.8$ eV) that expands through a nozzle into a vessel at low pressure, typically 0.2 mbar. The arc consists of four insulated plates, each with a 3 mm diameter hole. In this way a channel of 40 mm length is created. Three cathodes are positioned concentrically around the channel. The last plate, in which the nozzle is placed, acts as the anode. The nozzle has a straight channel with a diameter of 6 mm and a length of 10 mm. The last part of the nozzle (5 mm) makes an angle of 45° with the channel.

A schematic view of the laser-induced fluorescence setup is depicted in figure 1. A single-mode cw external cavity diode laser (EOSI LCU 2010M), delivering about 10 mW of radiation, is used to excite Ar* atoms in the expanding thermal plasma. The laser is tuned to the $1s_5 \rightarrow 2p_9$ transition at 811.53 nm or to the $1s_4 \rightarrow 2p_7$ transition at 810.37 nm[5]. The velocity along the laser beam, w_z, of the group of atoms in the metastable $1s_5$ and resonant $1s_4$ states absorbing the laser photons at frequency ν is deduced from the relation

$$w_z = c\frac{\nu - \nu_0}{\nu_0} \tag{8}$$

where ν_0 is the transition frequency for atoms at rest and c is the speed of light. In one configuration the laser beam travels in the opposite direction to the plasma propagation and

[5] For the transitions we use the Paschen notation [24]. The metastable $^3P_2$ and resonant $^3P_1$ levels are also known as the $1s_5$ and $1s_4$ levels in the Paschen notation and $4s[3/2]^o_2$ and $4s[3/2]^o_1$ in the Racah notation [25].

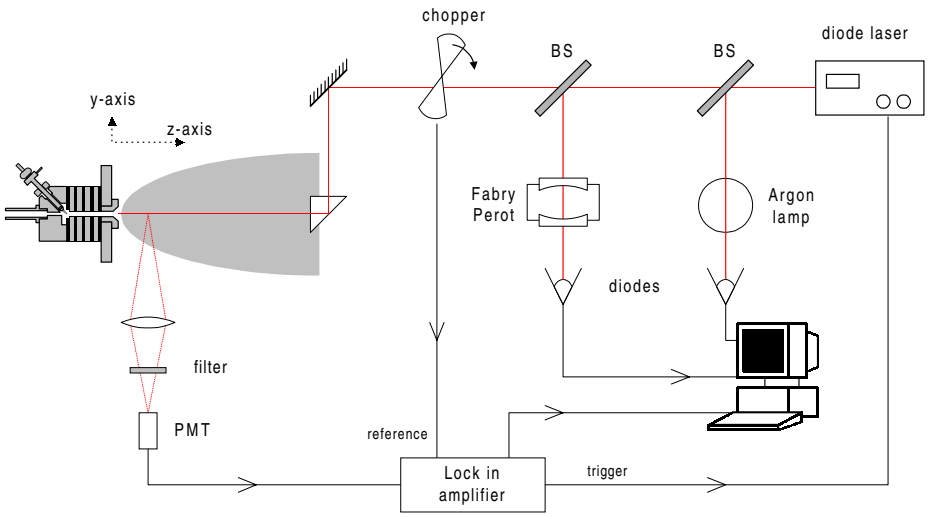

Figure 1. Schematic view of the experimental setup with which the LIF experiments are performed. The cascaded arc in which the thermal plasma is produced can be moved in the z-direction as well as in the y-direction. The fluorescence radiation is detected under 90°, i.e. the optical axis of the collection optics is in the x-direction.

excites the atoms on the centre z-axis of the expansion. In another configuration the beam is directed perpendicular to the propagation direction of the plasma jet. In this case the radial velocity of the atoms excited at different radial positions (y-axis) in the jet is monitored. The laser light is chopped at a frequency of about 800 Hz and the laser-induced fluorescence signal is detected under 90° (i.e. along the x-axis) with a photomultiplier tube (PMT). A high pass filter (λ cut-off 780 nm) placed between the plasma and the detector avoids saturation of the detector due to the emission of the plasma. A slit in front of the detector determines the spatial resolution of the experiment to 2 mm in both z- and y-directions. The laser beam diameter $d = 2$ mm determines the resolution in the third direction. The signal from the PMT is analysed with a lock-in amplifier with an integration time of 500 ms. The signal of the chopper is used as a reference signal for the lock-in amplifier. Part of the laser light is used to measure simultaneously the absorption profile of argon atoms in a low-pressure argon lamp ($T \approx 600$ K) and the transmission of a Fabry–Perot etalon. The three signals are recorded simultaneously with a 12 bits 200 kHz analogue-to-digital converter (National Instruments PCI-6023E). The tuning of the laser is controlled by the lock-in amplifier via a voltage supplied to the piezo connected to the end mirror of the external cavity of the diode laser. In this way, mode hop free scans of a few wavenumbers can be recorded. The line width of the laser is of the order of 1 MHz, much narrower than the line width of the recorded Ar transition in the expanding plasma and low-pressure argon lamp. The frequency shift between the absorption in the lamp and the LIF signal from the plasma is directly related via (8) to the velocity of the Ar atoms in the expanding plasma. The simultaneously recorded Airy-type transmission of the Fabry–Perot etalon is used to linearize the frequency axis.

The measurements presented here relate to the following standard conditions: a current of 40 A is drawn through the arc and an argon flow rate of 3.0 slm (standard litre per minute) is applied through the channel. A flow of 0.12 slm H_2 is added to the argon flow to decrease the ion density, and thus the metastable density, in order to avoid any significant diminution of the laser intensity due to absorption by metastable atoms present on the laser beam trajectory before reaching the excitation volume. With about 40 mW cm^{-2} laser fluence, the total saturation condition was fulfilled and the laser power was stationary along its trajectory, resulting in a frequency independent laser power in the excitation volume. Also, H_2 quenches the Ar[4s] atoms present on the outside of the expanding jet and therefore avoid the reabsorption of the LIF photons by these atoms, before reaching the detector. The influence of molecular hydrogen on the very fast ionization loss in an expanding argon/hydrogen plasma has been reported by Meulenbroeks *et al* [26]. The electron and argon ion densities are reduced due to charge exchange of Ar^+ with molecular hydrogen, followed by dissociative recombination of the ArH^+ ion forming Ar and excited atomic hydrogen. This leads to an ionization degree of less than 1%.

LIF measurements at different axial (z) positions have been performed in the expanding argon plasma jet for two different background pressures, i.e. 20 and 100 Pa, and on two different Ar[4s] $\rightarrow$ Ar[4p] transitions, i.e. $1s_5 \rightarrow 2p_9$ and $1s_4 \rightarrow 2p_7$. From the spectral profiles of the recorded signals both the temperature and the average velocity of the argon atoms are determined. Mainly the results on the $1s_5$ state, the lowest metastable state, will be discussed since the velocity distributions of the $1s_4$ state, the lowest resonant state, showed no significant difference with the former one. In figure 2 two velocity distributions are shown measured at $z = 60$ mm. One is recorded after excitation of the $1s_5 \rightarrow 2p_9$ transition (open squares), and one after excitation of the $1s_4 \rightarrow 2p_7$ transition (full squares). In both cases the same experimental plasma conditions were used. The small differences could also be attributed to a small difference in position at which the two spectra were recorded. The day-to-day reproducibility of the position of the plasma source in the z-direction is of the order of 1 mm.

The gas flow was slightly different than that used in the study of the transport of hydrogen atoms in an argon/hydrogen

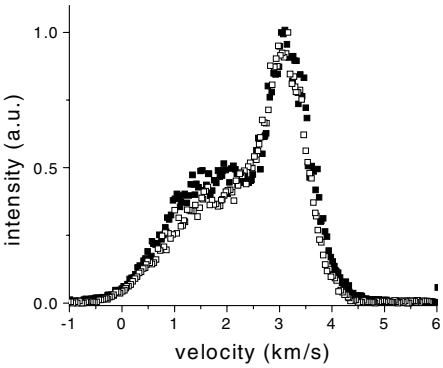

Figure 2. Axial velocity of atoms in the $Ar^*(^3P_2)$ metastable state (open squares) and the $Ar^*(^3P_1)$ resonant state (full squares) recorded at $z = 60$ mm. The arc was operated under standard conditions (3 slm Ar, 0.12 slm H_2, $I_{arc} = 40$ A) and the background pressure was set to 20 Pa.

expanding plasma jet during which the Rayleigh measurements were performed [27]; 3.43 slm argon and 0.07 slm hydrogen. Corrections were made for the small differences in flow when the neutral density profile was used in the data analyses reported here.

4. Results and discussion

In figure 3 the measured axial velocity distribution functions are shown, recorded at six different z-positions at a pressure of 20 Pa after excitation of the $Ar^*(1s_5) \rightarrow Ar^*(2p_9)$ transition. The laser frequency is converted to the velocity along the laser propagation direction by using (8). Although the measured spectra originate from Ar metastables, it will be argued that the velocity distributions image the velocity distributions of the ground-state Ar atoms.

4.1. Interpretation of the LIF spectra

Argon atoms in the long-lived 4s states that are used for the determination of velocity profiles are formed in a three-particle recombination process

$$Ar^+ + e + e \rightarrow Ar^* + e \tag{9}$$

and via radiation trapping that converts ground-state argon atoms to excited resonant Ar[4s] states: $Ar + h\nu \leftrightarrow Ar^*$ (*vide infra*). It is well established that all Ar^* atoms produced in the higher excited states by the three-particle recombination (equation (9)) cascade down to the 4s states [28, 29]. We will first discuss conditions under which the velocity distribution profile of these long-lived atoms is identical to that of the ground-state argon atoms. To have an idea about the relative importance of the different collisional processes, we calculated for background pressures of 20 Pa and 100 Pa the mean distances, that the different species in the jet can travel along the z-axis before having a collision with an Ar atom. We consider a cross section of 2×10^{-19} m^2 for Ar–Ar collisions and a cross section of 1×10^{-18} m^2 for both Ar^+–Ar and Ar[4s]–Ar collisions (see [30] for collisions concerning Ar and Ar^+; the cross section for Ar[4s] atoms and Ar^+ ions are discussed in section 4.2). We also suppose that at any z, the electron density

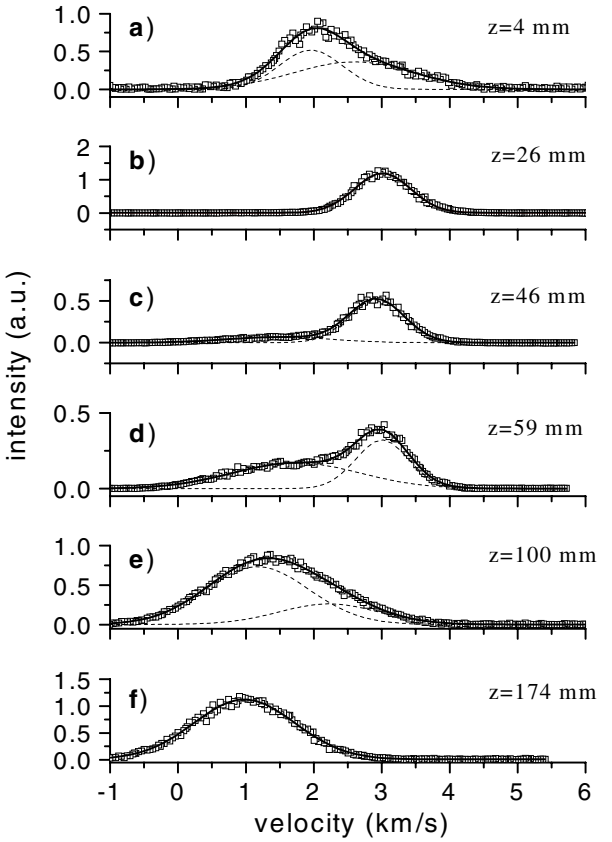

Figure 3. Axial velocity distributions recorded at six different z positions. The arc was operated at standard conditions and a flow of 3 slm argon with 0.12 slm H_2 was applied. The background pressure was set to 20 Pa. The full curves show the result of the fit. The broken curves show the individual Gaussian profiles.

will be about 100 times smaller than the argon density [27]. The argon density is constructed from Rayleigh measurements [27]. T_g and w_z are assumed to be equal to the temperature and mean velocity of the metastable atoms deduced from velocity profiles at different positions. The calculated mean distances, λ_{00}, λ_{i0} and λ_{m0}, in the laboratory frame, that an Ar, Ar^+ or Ar[4s] can travel along the z-axis before having a collision with an argon atom, using the following relation

$$\lambda = \frac{w_z}{n\sigma w_{th}} \tag{10}$$

are shown in figure 4(a) (20 Pa) and 4(b) (100 Pa). The thermal velocity w_{th} is deduced from T_g according to

$$w_{th} = \sqrt{\frac{2kT_g}{m}}. \tag{11}$$

4.2. Kinetics of the Ar[4s] atoms

To consider the kinetics of the four Ar[4s] states, we must first remember that the three-particle recombination process is instantaneous, and thus the argon atoms in the metastable and resonant states formed in this process image in the first instance the velocity distribution of the ions. But, the cross

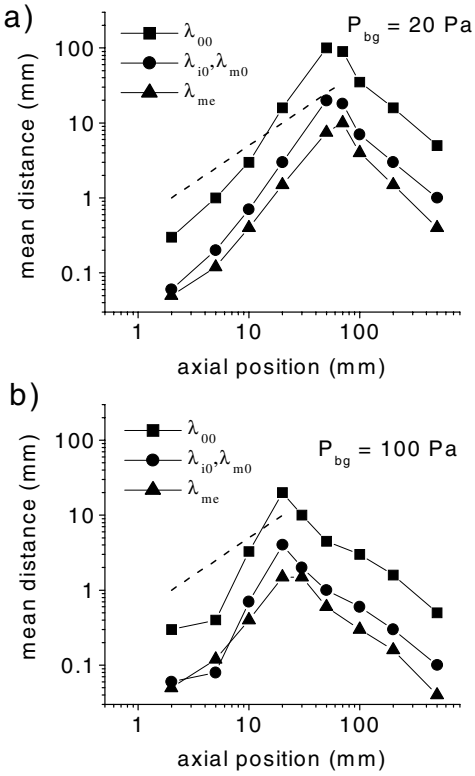

Figure 4. The mean distance an Ar, Ar^+ and Ar^* can travel along the z-axis before colliding with an argon atom at (a) 20 Pa and (b) 100 Pa background pressure. λ_{me} denotes the mean distance an Ar[4s] atom can travel along the z-axis before being transfered by collisions with electrons to an adjacent Ar[4s] state. The broken line indicates the typical gradient length L_n.

section for collisions of Ar^+ ions with argon atoms, including both charge transfer and elastic collisions, is about 10^{-18} m^2 [30]. Consequently, as one can see in figure 4(a), for $z <$ 20 mm, the path length of the ions, λ_{i0}, is smaller than 2 mm. This means that ion–neutral collisions are fast enough to equilibrate the velocity distribution of the ions with argon atoms. We therefore assume that in view of the smallness of λ_{i0} compared with the local gradient lengths, the Ar^+ ions and Ar atoms will be in equilibrium at these positions and further downstream. However, at short distances from the exit of the nozzle ($z <$ 16 mm at 20 Pa and $z <$ 8 mm at 100 Pa) we observe a forward peaking of the velocity distribution (see figure 3(a)). This forward peaking has already been reported in, e.g. time-of-flight measurements on a plasma created from a hollow cathode arc [31]. We here tentatively attribute the fast component to metastable atoms born from recombination of Ar^+ ions accelerated by an electric field generated from the gradient of the charge density in the expanding jet. The amplitude of this field is given by the Boltzmann relation [32]

$$E(z) = \hat{T}_e \frac{\nabla n_e}{n_e}. \tag{12}$$

Since the decay of n_e is similar to the decay of the neutral density [6, 27], for $z >$ 4 mm, $\nabla n_e/n_e$ is approximately $2/z$ and assuming $\hat{T}_e = 0.3$ eV, identical to the gas temperature, the amplitude of the electric field would be about 120 V m^{-1} at $z = 5$ mm and 60 V m^{-1} at $z = 10$ mm. In the valley and after the shock front the gradient and thus the fields are much smaller and reverse. Consequently the fast component should disappear as is observed.

Concerning Ar[4s] atoms, momentum transfer and metastability-exchange collisions with a cross section of about 10^{-18} m^2 will mix the $Ar^*(^3P_2)$ metastable and ground-state atoms. This collision cross section is determined from the diffusion coefficient $D = 1.7 \times 10^{20}$ molecule m^{-1} s^{-1} at 300 K [33] and the relation between D and the collision cross section deduced from [34]

$$D = \frac{3\pi}{16\sqrt{2}} \frac{\langle w \rangle}{\sigma}. \tag{13}$$

Here $\langle w \rangle$ is the mean velocity of argon atoms at 300 K. We can see in figures 4(a) and (b) that except for $30 < z < 100$ mm at 20 Pa and z around 20 mm at 100 Pa, the mean path length of metastable atoms, λ_{m0}, is comparable with, or smaller than the spatial resolution in our experiments. Similarly, the radiative lifetime of the resonant $Ar^*(^3P_1)$ and $Ar^*(^1P_1)$ states is of the order of 10^{-8} s. However, under our experimental conditions, due to the radiation trapping [35], the effective lifetimes of these states becomes a few microseconds. Consequently, due to this effect, argon atoms transfer very efficiently between the ground state and these resonant states. As an example, at an argon density of 10^{20} m^{-3}, the mean free path of the resonant VUV photons is less than 0.1 mm. This means that the velocity distribution of the resonant $Ar^*(^3P_1)$ and ground-state atoms are identical. Also, collisions with electrons will transfer Ar[4s] atoms between the resonant $Ar^*(^3P_1)$ and metastable $Ar^*(^3P_2)$ states, via $Ar^*(^3P_2) + e \leftrightarrow Ar^*(^3P_1) + e$. The mean distance λ_{me} that Ar[4s] atoms can travel along the z-axis before being transferred to the adjacent state is determined with the relation $\lambda_{me} = w_z/(k_e \times n_e)$. For this reaction the rate coefficient k_e is about 2×10^{-13} m^3 s^{-1} [36]. Assuming an electron density with the same z dependence as Ar atoms but 100 times smaller, we calculated the mean path length of a metastable atom before suffering a collision with an electron for 20 Pa (see figure 4(a)) and 100 Pa (see figure 4(b)) background pressure. For both pressures λ_{me} is smaller than the typical gradient length $L_n = n/\nabla n$ (about $z/2$ at these positions). Also, considering the velocity of the expanding jet $w_z \approx 3$ km s^{-1}, from the microsecond range lifetime of the resonant states we can conclude that for most positions the argon atoms in the metastable and resonant levels are produced and lost locally [28]. We conclude that for $z > 20(8)$ mm at 20 (100) Pa, the velocity distribution function of argon atoms in the 4s states is perfectly similar to that of the ground-state atoms. They are born from Ar^+ ions already in equilibrium with argon ground-state atoms and they are strongly coupled to the ground-state atoms by collisional processes and radiation trapping. Close to the shock wave, located around $z = 70$ mm at 20 Pa and $z = 30$ mm at 100 Pa, the mean free path for the neutral–neutral collisions becomes larger than the gradient length L_n, which means that the velocity distribution of argon atoms can differ from a Gaussian distribution in this region.

4.3. Measured velocity distribution functions of the Ar[4s] atoms

The velocity distributions shown in figure 3 can thus be seen as velocity distributions of neutral Ar atoms. As discussed before,

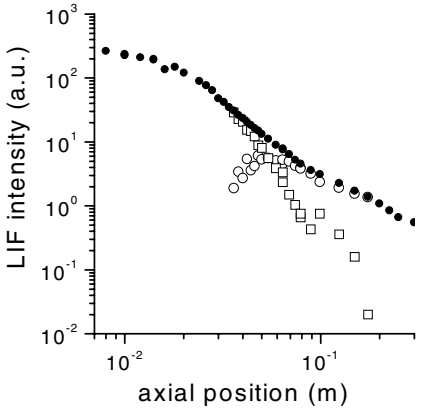

Figure 5. Contents of the two velocity distributions (open squares, fast component; open circles, slow component) describing the measured LIF signals. The total LIF signal is denoted by full circles.

the distributions for $z \leqslant 20$ mm can be distorted because of the presence of an accelerating E-field acting on Ar^+ ions (see figure 3(a)). At 20 Pa, for $20 < z < 30$ mm the measured fluorescence profile can be described to a good approximation with a Gaussian profile. After $z = 30$ mm, we start to observe clearly a non-Gaussian velocity distribution (see figure 3(c)) that can be described with two Gaussian profiles, each with their own average velocity and temperature. The relative amplitude of the slow but broader (and thus hotter) component increases with z. It will be argued later that background gas is responsible for this slow component, whereas the gas supersonically expanding from the cascaded arc is responsible for the fast and cold component of the velocity distribution. Around the stationary shock front the two features start to merge, but from the shape of the LIF profile it is clear that it still consists of two Gaussians (see figure 3(e)). For $z \geqslant 150$ mm, i.e. in the subsonic region of the expansion after the shock front, the velocity profile can be described with a single Gaussian again (see figure 3(f)).

In figure 5 the contents of both distributions in the 20 Pa case is shown (open symbols) as well as the total LIF signal (full symbols). At the start of the expansion, for $z < 20$ mm, the Ar[4s] density remains high and changes by only a factor of two. This is due to the fact that the production rate of Ar[4s] atoms, through electron–ion recombination, is proportional to $n_e^3 \times T_e^{-4.5}$ [37]. The rarefaction of n_e due to the expansion will be to some extent compensated by the diminution of T_e in this part of the plasma jet. Moreover here the production is still effective and contributes to the density. From $z = 20$ mm up to the shock wave, the density rarefaction effect is the main contributor to the decrease of the Ar[4s] density. However, the density drops slightly faster than with $1/z^2$, since the production via three-particle recombination decreases.

4.4. Axial average velocity and temperature

In figures 6(a) and 6(c) is shown the average velocity $\bar{v}$ of the Ar metastables along the z-axis. From the LIF traces of the measurements, the average velocity is determined from the calculation of the first moment of the velocity distribution

$$\overline{v} = \int v f(v)\,\mathrm{d}v \Big/ \int f(v)\,\mathrm{d}v \tag{14}$$

and is depicted with full cirles. In the range 32 mm $\leqslant z \leqslant$ 150 mm the measurements are also fitted with two Gaussians (open squares and circles). The area of the two Gaussians is a measure of the relative contents of the two velocity distributions (see figure 5). The width of the velocity distribution is a measure of the heavy-particle temperature in the moving frame of the expanding plasma jet. Since the velocity distribution is Maxwellian, the temperature is defined and related to the second moment, i.e.

$$\overline{v^2} = \int (v - \overline{v})^2 f(v)\,\mathrm{d}v \Big/ \int f(v)\,\mathrm{d}(v) \tag{15}$$

via the relation $kT = \frac{1}{2} m_{\mathrm{Ar}} \overline{v^2}$. The results are shown in figures 6(b) and 6(d). If two Gaussians are used in the fit, the temperatures are deduced from the width of the profiles. In this case the 'average' temperature, depicted with full circles, is calculated from the density-weighted temperature, i.e. $T = (n_1 T_1 + n_2 T_2)/(n_1 + n_2)$, in which n_1 and n_2 are the relative LIF intensities shown in figure 5.

The full curves in the figures 6(a) and 6(c) and figures 6(b) and 6(d) are calculated velocities and temperatures, using (2), (3) and (4). In all four cases $\gamma = 1.4 \pm 0.1$, $z_0 = 0.002 \pm 0.001$m, and $T_0 = 5600$ K, i.e. $c_{s_0} = 1270$ m s^{-1} is used. The adiabatic constant γ proves thus to be lower than that of a mono-atomic gas, i.e. $\frac{5}{3}$. This lower value may be due to finite ionization [38]. However, in the case of an Ar–H_2 mixture the ionization degree is low [27]. Therefore, departure from an adiabatic cooling in the supersonic domain of the jet most probably originates from heat transfer, from both the source and the background, in view of the high plasma heat conductivity and viscosity. T_0 is smaller than the temperature in the source T_s since the plasma already expands in the nozzle (due to our nozzle geometry, see section 3), before $z = 0$.

In figures 6(a) and 6(c) the crosses depict the sound velocity calculated using (1) and the temperatures of figures 6(b) and 6(d), respectively. The values in these figures show that for both background pressures the plasma is accelerated to about six times the speed of sound, i.e. $M = 6$. The good agreement of our experimental results on average velocity and temperature with the calculations in which we describe the thermal plasma expansion as if it is a hot neutral gas expansion with a slightly different adiabatic constant, shows the validity of this approach.

4.5. Behaviour of the forward flux in the expanding plasma jet

Using the total neutral argon atom density data from the Rayleigh measurements [27] and the velocity data of figure 6(c), the axial flux density as a function of distance from the source is determined for a background pressure of 100 Pa (see figure 7). For the data in the shock we assume that the relative contents of the two velocity groups of argon metastables in their axial velocity profile (depicted with open circles and squares) image the density ratio of the two velocity groups of the ground-state argon atom density. A fit using (2)

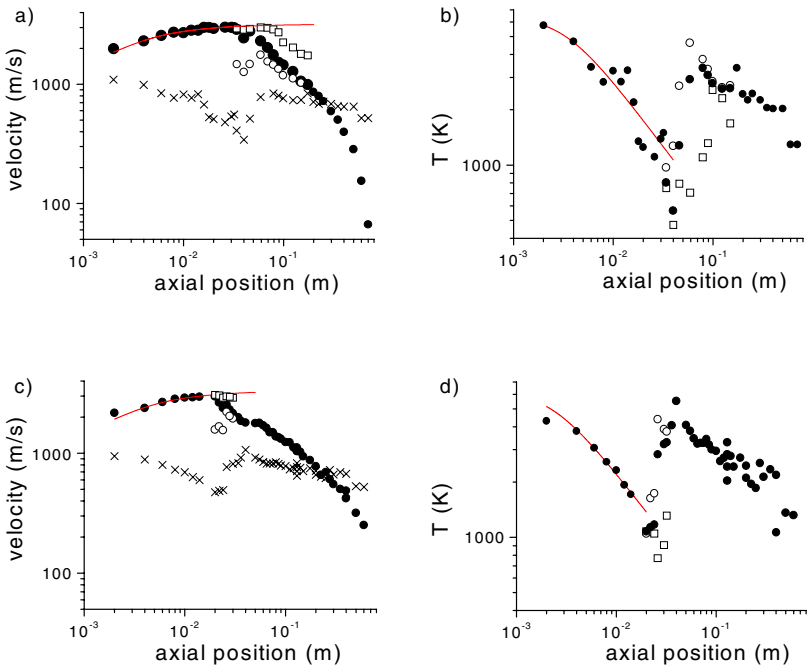

Figure 6. Axial average velocity (a) and (c) and temperature (b) and (d) measured as a function of the distance from the arc outlet at $P_{bg} = 20$ Pa (top) and $P_{bg} = 100$ Pa (bottom). Full circles are used to denote the results obtained from the first- and second-order moments, while open squares and circles are used to show the data analysed assuming two Gaussian profiles. The full curve is a fit through the data points up to the position where the velocity starts to decrease. The crosses in (a) and (c) depict the sound velocity calculated from the temperatures shown in (b) and (d) and using equation (1).

through the Rayleigh data showed that $n_0 = 3.2 \times 10^{22}$ m^{-3} and $z_0 = 3.8$ mm. From the result of figure 6(c) the flux density at the nozzle exit can now be deduced: $n_0 \times c_{s_0} = 4 \times 10^{25}$ m^{-2} s^{-1}. The flux at the start of the expansion can also be calculated from the area of the nozzle through which the plasma expands and the gas flows and assuming a homogeneous flux density distribution over the cross section, i.e. 5×10^{25} m^{-2} s^{-1}. Both are in good agreement with the measured flux density shown in figure 7, when we assume that the expansion in fact starts at a distance approximately the radius of the nozzle from the exit of the source, which is 3.0 mm. From that point the axial flux density on the centre axis decreases due to the increase in area of the jet. At the position where the density is minimal ($z = 20$ mm), the shock wave starts. The area is assumed not to increase over the thickness of the shock (see section 2.2). The decrease of the flux density should roughly equal the increase in area from the exit of the source to the area of the jet at $z = 20$ mm; i.e. a factor of 40. Our data in figure 7 show a difference of a factor of 20. The factor of two discrepancy could be explained by the fact that we do not take into account that the density distribution over the jet diameter can change while the jet expands. Preliminary results of calculations based on a hydrodynamic model, show that at a background pressure of 100 Pa the flow behind the first shock re-expands [39]. At elevated background pressures the pressure in the jet adapts to the background pressure via several compression stages. The plateau around $z = 45$ mm in the velocity measurements, shown in figure 6, is the onset of this effect.

Analysis of flow patterns by PHOENICS shows that behind the shock front the area of the jet is approximately

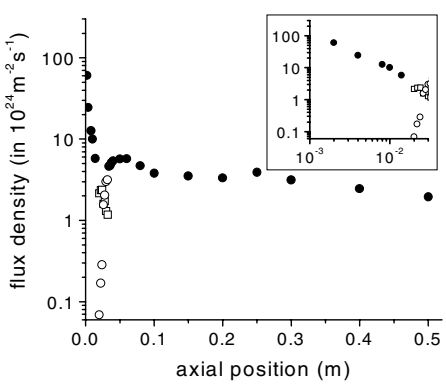

Figure 7. Total flux density of argon atoms on the axis of the Ar/H_2 expanding plasma jet at a background pressure of 100 Pa. The same symbols are used as in figure 6. The inset depicts the first 30 mm in a log–log plot to show more clearly the behaviour of the flux in the supersonic region of the plasma jet.

constant (surounded by recirculating vortices). For $z > z_m$ the flux density, i.e. $n \times w_z$ should also be about constant. Since the density is inversely proportional to the temperature at constant pressure, this would mean that in this part of the jet the velocity and temperature decrease equally fast. This proves indeed to be the case (see figure 8).

4.6. Radial average velocity and temperature

The radial average velocity as a function of the distance y from the centre z-axis at $z = 50$ mm is shown in figure 9. The same experimental conditions have been used as during

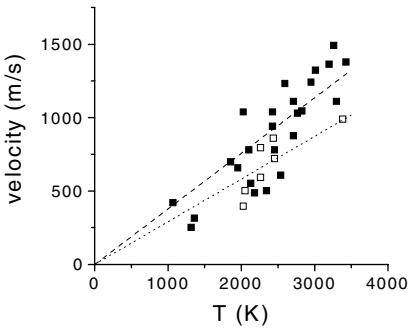

Figure 8. The measured axial average velocity as a function of the parallel temperature in the subsonic part of the expansion for 20 Pa (open squares) and 100 Pa (full squares). The dotted and dashed lines are linear fits through the data points (including 0, 0), for 20 Pa and 100 Pa background pressure, respectively.

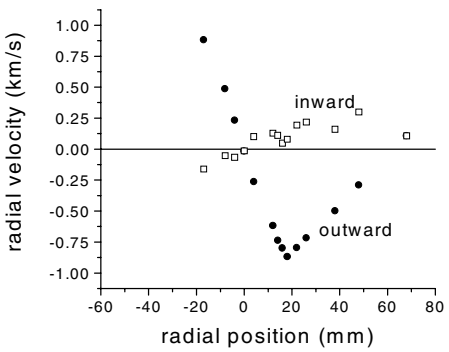

Figure 9. The radial average velocity of the two distributions as a function of the radial distance from the jet centre line (z-axis). The velocities are determined from a fit of the LIF signal using two Gaussian profiles (see figure 10). The axial z-position is 50 mm, i.e. in the shock region, and the background pressure is 20 Pa. The inward directed velocity is denoted by open squares, the outward directed velocity with full circles.

the axial measurements, i.e. background pressure of 20 Pa, current through the arc of 40 A, and a flow of 3 slm argon plus 0.12 slm H_2. As for the axial velocity distributions, also in radial direction non-Gaussian velocity distributions are measured (see figure 10). In this case, however, the peaks of the two velocity distributions are located on opposite sides of the zero velocity position, determined from the absorption feature measured in the low pressure Ar lamp. This is true except on the centre axis where both distributions have zero average radial velocity, as expected (see figure 10(b)). The fact that close to the jet boundary the two velocity groups have opposite mean velocity means that at every $y \neq 0$ position one velocity group is directed inward, and one velocity group is directed outward.

In going from the centre z-axis along the radius, the stream lines fan out, making an angle with the plane perpendicular to the z-axis. This angle increases up to the boundary of the barrel shock structure on the side of the expansion. In a 45° expansion the outer boundary of the jet would be at $y = z$, i.e. $y = 50$ mm during the experiment discussed here. The shock wave thickness is roughly 30 mm at 20 Pa, deduced from Rayleigh measurements [27]. This means that the maximum radial velocity would be reached at about $y = 20$ mm, which

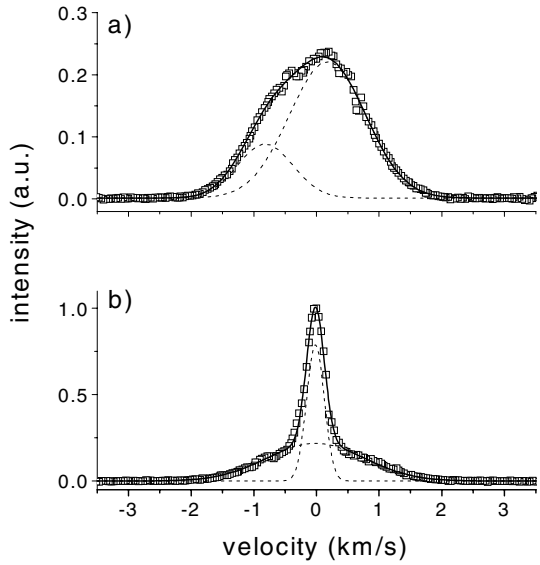

Figure 10. Radial velocity distributions recorded at two different y-positions, i.e. (a) at $y = 22$ mm and (b) at the centre z-axis ($y = 0$ mm). The axial z-position is 50 mm. The arc was operated at standard conditions and a flow of 3 slm argon with 0.12 slm H_2. The background pressure was set to 20 Pa. The full curves show the result of the fit. The broken curves show the individual Gaussian profiles.

is in good agreement with our measurements. At this distance the velocity of the Ar atoms along the stream line is about 2.5 km s^{-1} (see figure 6(a), taking into account that the distance from the point where the expansion starts is larger than 50 mm at $z = 50$ mm, $y = 20$ mm). This means that the radial component of this velocity at $y = 20$ mm and $z = 50$ mm on the y-axis is about 0.93 km s^{-1}, in good agreement with our measurements.

In figure 11 the temperature of the two distributions, as determined from the width of each velocity group, is shown as function of the y-position. The distribution that belongs to the outward pointing velocity, has a lower temperature than the inward moving distribution. This can be understood from the fact that the outward high w_y-group belongs to the expanding jet atoms. It is therefore obvious that in the central part of the jet the dispersion of their radial velocity will be very small. This results in a low value of the perpendicular temperature for this group of atoms, as can be seen in figure 11. On the contrary, the low w_y group results from background gas that entered the supersonic part of the expanding plasma jet. Given that the density of Ar atoms of the expanding jet is at least two orders of magnitude larger than the density of Ar^+ ions or Ar[4s] atoms, these entering atoms will preferentially collide and exchange momentum and energy with ground-state Ar atoms. However, at $z = 50$ mm the mean free path of these entering atoms, before they collide with an argon atom of the expanding jet, is comparable with the size of the jet. Therefore, the entering atoms can deeply penetrate the jet. Atoms passing the centre axis of the jet before arriving at the measurement point have a larger probability of colliding than those entering from the side of the measurement point. Still, the mean velocity of these bulk atoms will be directed towards the core of the jet. Also, at smaller values of y, the distribution will be broader, resulting in

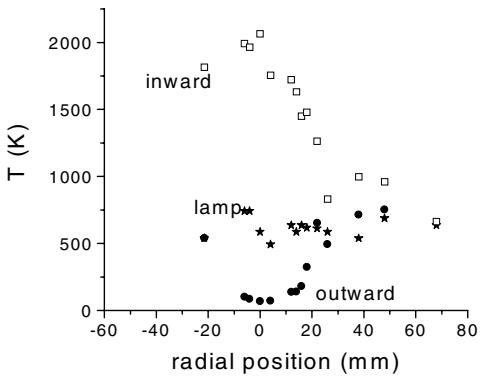

Figure 11. The radial temperature of the Ar atoms as a function of the distance from the centre z-axis. The temperature is determined from the width of the two Gaussian LIF profiles (see figure 10). The axial z-position is 50 mm and the background pressure 20 Pa. The temperature of the inward moving distribution is denoted by open squares, the temperature of the outward moving distribution by full circles. The temperature deduced from the line profile in the lamp is given as a reference ($*$).

a higher perpendicular temperature. This is also a consequence of the larger time atoms with smaller w_y spend inside the jet, where they can suffer elastic collisions with the fast Ar atoms of the jet, but also the less important, charge exchange with Ar^+ ions and metastability exchange with Ar[4s] atoms.

A sign of the penetration of neutral argon atoms is the presence of a slow component in the axial velocity on the centre z-axis, as shown in figures 3(e) and 6(a), in the case of 20 Pa background pressure. The argon atoms that constitute the supersonic distribution (open squares) collide with atoms penetrating the Mach disc from the subsonic region and as a consequence the fast distribution gives rise to a slow distribution (open circles). However, at $z \approx$ 90 mm, next to this effect, the whole supersonic distribution starts to decelerate, which is not in agreement with the bi-modal approximation (see section 2.2). This effect could be connected to a third velocity component in the VDF, discovered in the supersonic gas jet at low pressure [40, 41]. We believe that atoms that penetrate the jet from the side are responsible for this effect. In the 100 Pa case this effect should occur over a much shorter range, which cannot be resolved with our spatial resolution.

This invasion of background gas was already predicted by Fenn and Anderson [42] in 1966 and deduced from mass spectrometric measurements by, e.g. Campargue [43]. In the work of Campargue the discrepancy between the measured and theoretically predicted total flow rate through a skimmer positioned in an expanding gas flow (the predicted value was always lower than the measured value) is explained by a possible invasion of background gas in the barrel shock structure. It was also shown that this effect could be used for the separation of mixtures of different gasses and isotopes. Our LIF measurements are a direct indication that invasion of the background gas is indeed present. This invasion will be the most prominent in front of the stationary shock wave, where the mean free path for neutral–neutral collisions in the 20 Pa case is around the radius of the jet. In the case of 100 Pa, the mean free path is slightly less than the radius of the jet, and the effect of invasion is expected to be less.

5. Conclusions

Velocity and temperature measurements using the laser-induced fluorescence technique on metastable argon in an expanding thermal argon/hydrogen plasma have been presented. We demonstrated that the velocity distribution profile of these metastable atoms reflects the velocity distribution of the ground-state argon atoms. The results show that in the supersonic part of the expansion the velocity and temperature behaviour can be described as a hot neutral gas expansion with a smaller adiabatic constant, i.e. 1.4 instead of $\frac{5}{3}$. In the first part of the supersonic expansion both parameters behave independently of the background pressure, as is expected for a supersonically expanding gas.

Previously reported Rayleigh measurements on total argon density and laser-induced fluorescence data on the temperature and velocity in the subsonic part of the expansion, which are presented here, show that the plasma jet diameter behind the shock stays almost constant, as was predicted by analysis of flow patterns by PHOENICS.

The velocity distributions of the argon atoms in axial and radial directions clearly show a departure from thermodynamic equilibrium. The measured non-Maxwellian distributions can well be described with the sum of two Maxwellian distributions. It is concluded that one distribution originates from gas accelerated and cooled in the supersonically expanding plasma jet, while the other one originates from background gas penetrating in the valley of the barrel shock structure.

Acknowledgments

The authors would like to thank Professor M C M van de Sanden for stimulating discussions and M J F van de Sande, A B M Hüsken and H M M de Jong for their skilful technical assistance. This work is part of the 'Stichting voor Fundamenteel Onderzoek der Materie (FOM)'-EURATOM agreement and the research program of FOM (project FOM-95RG09), which is financially supported by the 'Nederlandse Organisatie voor Wetenschappelijk Onderzoek (NWO)'.

References

[1] Miller J C and Hagelund R F 1998 *Experimental Methods in Physical Science* vol 30 (San Diego: Academic)
[2] Hantzsche E 1990 *Contr. Plasma Phys.* **30** 575
[3] Campargue R 1984 *J. Phys. Chem.* **88** 4466
[4] Aithal S M, Subramaniam V V and Babu V 1999 *Plasma Chem. Plasma Proc.* **19** 487
[5] Gielen J W A M, Kessels W M M, van de Sanden M C M and Schram D C 1997 *J. Appl. Phys.* **82** 2643
[6] van de Sanden M C M, de Regt M J and Schram D C 1994 *Plasma Sources Sci. Technol.* **3** 501
[7] van de Sanden M C M, van den Bercken R and Schram D C 1994 *Plasma Sources Sci. Technol.* **3** 511
[8] van de Sanden M C M, de Regt J M and Schram D C 1993 *Phys. Rev.* E **47** 2792
[9] Meulenbroeks R F G, van Beek A J, van Helvoort A J G, van de Sanden M C M and Schram D C 1994 *Phys. Rev.* E **49** 4397
[10] Meulenbroeks R F G, Engeln R A H, van der Mullen J A M and Schram D C 1996 *Phys. Rev.* E **53** 5207
[11] Mazouffre S, Boogaarts M G H, van der Mullen J A M and Schram D C 2000 *Phys. Rev. Lett.* **84** 2622
[12] Mazouffre S, Boogaarts M G H, Bakker I S J, Vankan P, Engeln R and Schram D C 2001 *Phys. Rev.* E **64** at press

[13] van der Heijden H W P, Boogaarts M G H, Mazouffre S, van der Mullen J A M and Schram D C 2000 *Phys. Rev.* E **61** 4402
[14] Gielen J W A M, van de Sanden M C M and Schram D C 1996 *Appl. Phys. Lett.* **69** 152
[15] Ashkenas H and Sherman F S 1996 *Proc. Rarefied Gas Dynamics* vol 4, ed J H de Leeuw (New York: Academic)
[16] Miller D R 1988 *Atomic and Molecular Beam Methods* ed G Scoles (Oxford: Oxford University Press)
[17] Schram D C, Mazouffre S, Engeln R and van de Sanden M C M 2001 *Atomic and Molecular Beams* ed R Campargue (Berlin: Springer)
[18] Landau L D and Lifshitz E M 1987 *Fluid Mechanics* 2nd edn (London: Pergamon)
[19] Mott-Smith H M 1951 *Phys. Rev.* **82** 885
[20] Muckenfuss C 1960 *Phys. Fluids* **3** 320
[21] Glansdorff P 1962 *Phys. Fluids* **5** 371
[22] Kessels W M M, Leroux A, Boogaarts M G H, Hoefnagels J P M, van de Sanden M C M and Schram D C 2001 *J. Vac. Sci. Technol.* A **19** 467
[23] van de Sanden M C M, de Regt J M, Jansen G M, van der Mullen J A M, Schram D C and van der Sijde B 1992 *Rev. Sci. Instrum.* **63** 3369
[24] Wiese W L, Smith M W and Miles B M 1969 *Atomic Transition Probabilities* vol II (NBS–US Department of Commerce)
[25] Wiese W L, Brault J W, Danzmann K, Helbig V and Kock M 1989 *Phys. Rev.* A **39** 2461
[26] Meulenbroeks R F G, Engeln R A H, Box C, de Bari I, van de Sanden M C M, van der Mullen J A M and Schram D C 1995 *Phys. Plasmas* **2** 1002
[27] Meulenbroeks R F G, Engeln R A H, Beurskens M N A, Paffen R M J, van de Sanden M C M, van der Mullen J A M and Schram D C 1995 *Plasma Sources Sci. Technol.* **4** 74
[28] Buuron A J M, Otorbaev D K, van de Sanden M C M and Schram D C 1994 *Phys. Rev.* E **50** 1383
[29] Benoy D A, van der Mullen J A M, van de Sanden M C M, van der Sijde B and Schram D C 1993 *J. Quant. Spectrosc. Radiat. Transfer* **49** 129
[30] Phelps A V 1994 *J. Appl. Phys.* **76** 747
[31] Theuws P 1981 *PhD Thesis* Eindhoven University of Technology
[32] Chen F F 1985 *Introduction to Plasma Physics* (New York: Plenum)
[33] Kolts J H and Setser D W 1978 *J. Chem. Phys.* **68** 747
[34] Hirschfilder J D, Curtiss C F and Bird R B 1967 *Molecular Theory of Gases and Liquids* (New York: Wiley)
[35] Holstein T 1951 *Phys. Rev.* **83** 1159
[36] Lymberopoulos D P and Economou D J 1993 *J. Appl. Phys.* **73** 3668
[37] Bates D R and Kingston A E 1964 *Proc. Phys. Soc. (London)* **83** 43
[38] Burm K T A L, Goedheer W J and Schram D C 1999 *Phys. Plasmas* **6** 2622
[39] Chazot O private communication
[40] Pham-Van-Diep G, Erwin D and Muntz E P 1989 *Science* **245** 624
[41] Ramos A, Maté B, Tejeda G, Fernández J M and Montero S 2000 *Phys. Rev.* E **62** 4940
[42] Fenn J B and Anderson J B 1966 *Proc. Rarefied Gas Dynamics* vol 2, ed J H de Leeuw (New York: Academic)
[43] Campargue R 1970 *J. Chem. Phys.* **52** 1795